International Journal of GEOMATE, Nov., 2018 Vol.15, Issue 51, pp.180-187
Geotec., Const. Mat. & Env., DOI: https://doi.org/10.21660/2018.51.02150
ISSN: 2186-2982 (Print), 2186-2990 (Online), Japan

MONITORING THE TRIGGERING OF LIQUEFACTION USING IMAGE PROCESSING

*Erica Elice Saloma Uy[1], Toshihiro Noda[2], Kentaro Nakai[3] and Jonathan Rivera Dungca[4]

[1]Graduate Student, De La Salle University, Philippines; [2,3] Nagoya Univesity, Japan; [4]De La Salle University, Philippines

*Corresponding Author, Received: 27 April 2018, Revised: 30 May 2018, Accepted: 18 June 2018

ABSTRACT: In recent studies triggering or initiation of liquefaction is usually performed to characterize the potential of the soil to liquefy. Its behavior before, during and after liquefaction in a laboratory test needs to be understood. Image processing was implemented to monitor the triggering of liquefaction and estimate the cyclic shear strain that would trigger liquefaction. Lucas and Kanade pyramidal optical flow algorithm were used to track the movement of the soil. A mirrorless camera was the instrument used. The strain-controlled consolidated undrained cyclic triaxial test was performed. The loose condition was tested at 2.4, 1.6 and 0.8 mm strain amplitudes. The confining pressures used were 50, 100 and 200 kPa. Based on the results, the estimated values for the cyclic shear strain that would trigger liquefaction had a range of values due to the occurrence of non-homogeneous deformation. The minimum values were in agreement with the typical values while the maximum values were larger. For the behavior of the soil before, during and after liquefaction had occurred, the deformation behavior was different. More deformations were observed after the triggering of liquefaction.

Keywords: Cyclic Loading, Liquefaction, Optical Flow, Cyclic Shear Strain Triggering Liquefaction

1. INTRODUCTION

Liquefaction is a phenomenon that can be a result of earthquake shaking or other ground vibrations due to construction techniques such as blasting and soil compaction. It is susceptible to cohesionless soil especially when it is fully saturated with groundwater. As shaking occurs, soil experiences deformation and it is followed by the generation of excess porewater pressure from the groundwater. At this state, strength reduction has already occurred and soil behaves like a liquid. An extensive study on liquefaction has already been conducted to understand its behavior [1]-[3]. The area of research usually focuses on the investigation of the factors influencing liquefaction such as excess pore water pressure, shear strength and shear strain or deformation of soil [2]. The initiation or triggering of liquefaction is also an important area that needs investigation. There are at least two general methods for assessing the triggering of liquefaction. The first method is based on the field performance correlation of the parameters and observed field behavior determined from in-situ testing techniques [4]-[6]. The second method is based on the assessment of the soil tested in the laboratory [4]-[6]. The parameters obtained for both methods can be evaluated with respect to cyclic stress or cyclic strain approach [7]-[8]. For the two general methods in assessment, most studies focused on the evaluation of liquefaction resistance of the soil, the advantage between using field performance data to laboratory data and incorporating probabilistic and deterministic approaches in improving the assessment of liquefaction potential [5]-[8]. On the other hand, how the soil behaves before and after liquefaction had occurred needs further understanding. A technique that can be used in investigating the initiation of liquefaction is by image processing. In this technique, deformation measurements were carried out without any direct contact with the soil specimen [9]-[13]. This method was recently incorporated in a dynamic triaxial compression test. The particle image velocimetry (PIV) algorithm was applied in determining the axial and radial deformation of strain field. The information extracted from this non-contact measurement technique gave a strong experimental foundation to investigate the soil samples mechanical characteristics [12]. In another study, local properties of saturated Toyoura sand in undrained cyclic triaxial tests were observed [13]. A charged coupled device (CCD) camera was used to monitor the displacement. Based on their results, image processing can be used in monitoring the deformation of the soil under cyclic loading. It is the objective of this study to monitor the behavior of the soil before, during and after the triggering of liquefaction. A strain controlled consolidated undrained test was performed since the sand fabric has an effect towards the pore pressure buildup in a stress-controlled test [7]-[8]. In a cyclic strain approach, the cyclic shear strain that would trigger liquefaction (γ_{cl}) serves as an indication whenever liquefaction is attained. This parameter is compared to the cyclic shear strain (γ_c). When γ_c is greater than γ_{cl}, this is an indication that liquefaction has initiated [8]. In Fig.1, the change in pore water pressure ratio or the ratio of the excess pore water pressure and cell pressure is plotted against the γ_c, the minimum value of γ_{cl} is shown. This is the instance where the pore water pressure ratio is almost 0.95 or triggering of liquefaction is about to occur. Its typical value ranges from 0.4 to 3% [8]. At this point, the development of pore water pressure already occurred. Furthermore, movements of soil particles also occurred which can cause excess pore water pressure to accumulate. The γ_{cl} was also estimated using image processing. A mirrorless camera was used instead of using a high-speed camera because it is more cost-effective. Lucas and Kanade pyramidal optical flow algorithm were implemented and only 2-D image processing was performed [9], [16]-[17].

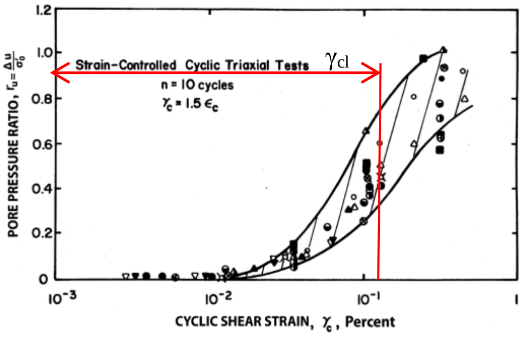

Fig.1 Pore water pressure ratio plotted against γ_{cl} [8]

2. IMAGE PROCESSING

2.1 Optical Flow

Optical flow is an algorithm that monitors the movements of a point of interest in an image. The algorithm specifically monitors the changes in grayscale values. In image processing, colored images are converted to grayscale images in order to avoid complexity in distinguishing the colors from each other [14]. In a colored image, each pixel can be described by red-green-blue (RGB) model and each color has its own pixel value. For grayscale images, it identifies the intensity of the light. Grayscale pixel values range from 0 to 255. Dark light intensity has a value of zero while bright light intensity has a value of 255. In order to determine the displacement at a certain time interval, searching for conjugate points by matching the gray level corners of the point of interest must be performed [15]. The changes in movements are indicated as:

$$\vec{\boldsymbol{v}} = (\boldsymbol{u_x}, \boldsymbol{v_y}) \tag{1}$$

where $\vec{\boldsymbol{v}}$ = velocity; u_x = x component and v_y = y component.

Lucas and Kanade pyramidal optical flow algorithm were implemented in the study. It is a feature-based technique that minimizes the residual function $\boldsymbol{\varepsilon}$ in order to extract image velocity $\vec{\boldsymbol{d}}$ at succeeding images. The algorithm incorporates least squares technique and a windowing method with image patches [16]. The algorithm has the following expression:

$$\boldsymbol{\varepsilon}(\vec{\boldsymbol{d}}) = \boldsymbol{\varepsilon}(\boldsymbol{d_x}, \boldsymbol{d_y}) = \sum_{x=u_x-\omega_x}^{u_x+\omega_x} \sum_{x=u_y-\omega_y}^{u_y+\omega_y} [\boldsymbol{I}(\boldsymbol{x},\boldsymbol{y}) \\ - \boldsymbol{J}(\boldsymbol{x}+\boldsymbol{dx}, \boldsymbol{y}+\boldsymbol{dy})]^2 \tag{2}$$

where $I(x, y)$ = First image with (x,y) pixel location; $J(x, y)$ = Second image with (x,y) pixel location; dx, dy = image displacement and ω_x, ω_y = are arbitrary numbers that ranges from 1, 2, 3 or more pixels.

2.2 Calibration and Capacity of the Camera

To ensure that the mirrorless camera can monitor the triggering of liquefaction, calibration and capacity check was performed. Calibration was performed to eliminate distortion from the camera, geometric distortion, and magnification from the triaxial cell and the water. Calibration was divided into two phases. For the first phase, the camera was calibrated to eliminate distortion by establishing the internal, external and distortion parameters. Internal parameters define the camera coordinate system. External parameters relate the camera's position and orientation with respect to the real world coordinate system. Calibration was implemented by first using a calibration grid as seen in Fig.2. It was used as a target in order to establish the parameters needed. This type of grid was used since having distinct and identifiable points can better establish the needed parameters [18]. The target must be positioned in the area where image processing will be applied. It must have a different orientation at every image taken. It must be within the range of +20 degrees. For the algorithm used for the calibration, a minimum of 5 images was taken to ensure a good calibration. Then the images taken were converted to grayscale and threshold was performed to extract the grid features of the calibration panel. The calibration axis was established in the image at the upper left corner of the grid. Lastly, internal, external and distortion parameters were estimated. For the second phase, a magnification factor was established to correct the geometric distortion and magnification from the triaxial cell and water. A straight edge block was used as seen in Fig.3 to determine the factor. This was confined to the triaxial cell and submerged with water. Its dimension is 10.0 cm x 7.0 cm. A straight edged block was used since it can be easily detected by the image processing routing called edge detection. This routine measures the dimension of the block and targets. Targets of different sizes as seen in Fig. 3 were placed on the block. The sizes are varied especially for the y-axis in order to check the amount of geometric distortion and magnification. The dimension of the targets is listed in Table 1. Magnification factor established for both the x and y-directions is 0.7036 and 0.8579, respectively. This factor was established by plotting the value of the true dimension against the actual measurement. The magnification factor is the slope of the plot. At this phase, the exact location and the camera settings were also established. The mirrorless camera was placed 42 cm away from the apparatus. It is located at the back of the equipment. This location was chosen to ensure that the position of the mirrorless camera will be fixed all throughout the experiment. Lighting condition was also controlled to ensure that there is an even distribution of light. Furthermore, the triaxial cell is made up of a plexiglass which can cause an inconsistent distribution of light towards the straight edge block. To address this, the black paper was placed in front of the apparatus.

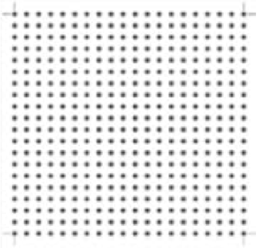

Fig.2 Calibration grid

Fig.3 Straight edged block

Table 1 Dimension of the targets

Target	Dimension (LxH) (cm)
1	0.7x1.0
2	0.7x1.0
3	0.7x0.7
4	0.7x2.0
5	0.7x0.5

The capacity of the mirrorless camera to measure deformation was also investigated. In a cyclic triaxial test, the sample to be tested has a cylindrical shape to simulate its geometry a rubber cylindrical dummy was used as a sample as seen in Fig.4. The sample was tested under a strain-controlled condition. The dummy was tested having 2.4, 2.0, 1.6, 1.2 and 0.8 mm strain amplitude (SA). The frequency ranged from 0.002 to 0.006 Hz. The rubber dummy is tested for two cycles to investigate if the mirrorless camera can capture the cyclic deformation. The lighting condition was also further improved while checking the capacity because the noise was experienced. To correct this, a spotlight was placed on top of the apparatus because the black paper was not enough to ensure that the rubber dummy has an even lighting condition. The measurements from the mirrorless camera were compared to the linear variable displacement transducer (LVDT). The target used for comparison is the top cap. Based on the results, the mirrorless camera can measure the strain amplitudes tested. Errors are mostly observed where the positive values shift towards the negative values.

Fig.4 Rubber dummy

3. EXPERIMENTAL PROGRAM

3.1 Sample Preparation

The sample used was the Mikawa number 6 sand. It is an artificially produced shaved sample in Nagoya, Japan and has high concentrations of silica and can be considered as silica sand. The sample can be classified as a coarse material which is vulnerable to liquefaction. It was used to ensure liquefaction can be achieved. Samples were prepared by air pluviation. Loose condition (S1) was prepared to have 30% as the target relative density. The sample preparation procedure was followed with respect to the Japanese Geotechnical Society (JGS) standard for sample preparation of coarse granular materials for the triaxial test (JGS 0530-2009) [19].

3.2 Cyclic Triaxial Test

The strain-controlled consolidated undrained test was implemented in the study. The procedure in JGS 0541-2009 was followed and the experiment was divided into three phases namely, saturation, consolidation and cyclic loading [19].

In the saturation phase, CO_2 was infiltrated into the sample in order to ensure that a fully saturated condition can be attained. The B-value or the ratio of the porewater pressure and the cell pressure was the parameter obtained after the desired cell pressure and back pressure to saturate the sample were reached. It served as the indicator for a fully saturated condition. The parameter must have a value of greater than or equal to 0.95. In the consolidation stage, the confining pressure applied was 50, 100 and 200 kPa. For the cyclic loading stage, the samples were cyclically loaded for 10 cycles and the strain amplitudes (SA) adopted was 2.4, 1.6 and 0.8 mm. The frequency was 0.004 Hz. A slow frequency was adopted to properly monitor the triggering of liquefaction. Furthermore, this ensures that there is a constant distribution of excess pore water pressure and vertical stress in the specimen. The mirrorless camera took pictures every 5 seconds.

4. CYCLIC SHEAR STRAIN THAT WOULD TRIGGER LIQUEFACTION

The γ_{cl} was estimated by checking the values of γ_c and its corresponding pore water pressure ratio when liquefaction was about to trigger. The pore water pressure ratio that has a value of 0.95 or greater is the state when liquefaction had already occurred [19]. On the other hand, the state when liquefaction was about to trigger was the instance right before liquefaction had occurred. The value of the pore water pressure ratio is close to 0.95 but not less than 0.90. In order to estimate the γ_{cl} from image processing (IP), the cyclic shear strain was first computed using the general engineering shear strain formula [20]. The image was divided into a 5 x 5-pixel mesh. The deformation in the x and y-directions were extracted with respect to the mesh size. The cyclic shear strain was computed assuming 2-dimensional plane condition using the following equation:

$$\gamma = \frac{1}{2}\left(\frac{\partial v}{\partial x} + \frac{\partial u}{\partial y}\right) \tag{2}$$

where $\frac{\partial v}{\partial x}, \frac{\partial u}{\partial y}$ = displacement gradient.

The γ_{cl} was monitored at the center (C). This location was further subdivided into the top (T), middle (M) and bottom (B) section as seen in Fig.5. In this study, curvature effect was not yet considered. That is why the values are estimated at the center. At this location, curvature effect is not severe as the other locations. The parameter was monitored at different sections in order to investigate how distributed the values are. To further investigate its distribution, the shear strain field was extracted and plotted in a color map.

In order to verify the results, the results from IP are compared to the results from the LVDT. From the data obtained from the LVDT, the shear strain was computed using the following equation [3], [7]:

$$\gamma = \varepsilon_a(1+\nu) \tag{3}$$

where ε_a = axial strain; ν = Poisson's ratio. The Poisson's ratio for saturated sand can be assumed to be 0.5.

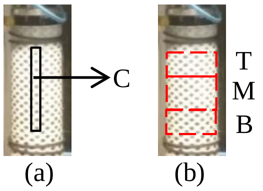

Fig.5 Monitored (a) location and (b) section

5. RESULTS AND DISCUSSION

The γ_{cl} was estimated for the loose condition. The confining pressure and strain amplitudes were varied to investigate if these have an effect towards the value of the parameter. The γ_c determined from IP was first verified by comparing it to the computed values from the LVDT. The LVDT used had a rated capacity of 20 mm, a sensitivity of 5 mV/V ±0.1 % and measurement uncertainty of within ±0.1 % of its rated capacity. A target was chosen to verify in order to compare the results. The target chosen was the top cap since it also moves in the same movement as the piston. As seen in Fig.6, a good agreement was observed. For the internal measurements seen in Fig.7, it can be observed that at the early stage of the experiment, the γ_c values from IP had a good agreement at the top section. For the middle section, values obtained from IP are smaller but it is larger compared to the bottom section. When liquefaction had occurred at this state the pore water pressure ratio is close to 1.0, a similar trend was observed for both the middle and bottom section. The top section on the other hand accumulated larger deformation at this state. In a typical cyclic triaxial test, deformation is assumed to be uniform. Based on the results of IP as seen in Fig.7, when an element or particle of soil is measured at different sections its deformation behavior exhibited a non-homogeneous trend. This is because the top and bottom sections are constrained by the cap and pedestal. The pore water pressure ratio generation with respect to the γ_c determined from the LVDT and IP was plotted as shown in Figs.8-10. Based on the results, prior to liquefaction the γ_c from IP had a good agreement with the top section. For the middle section values were smaller. This decrease in values was observed towards the bottom section. Once liquefaction was triggered, the γ_c, estimated from IP was varied in terms of the location where it was obtained. The γ_c at the top section is now larger while a similar trend was observed for the other two sections. A sudden increase in the pore water pressure ratio was observed for all conditions which are expected to occur in a loose sample.

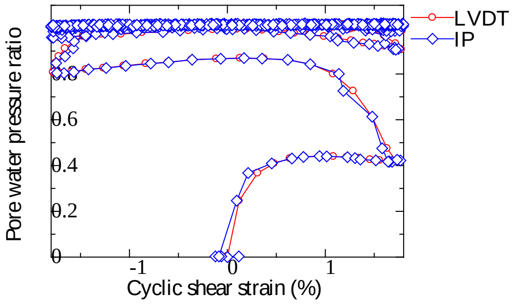

Fig.6 Comparison of the γ_c determined from LVDT and IP

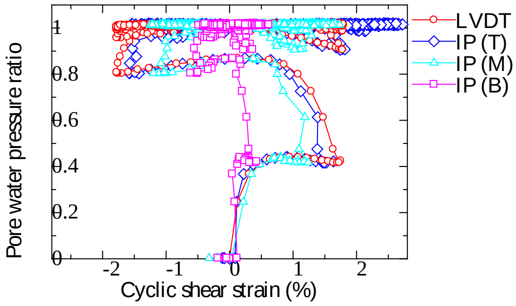

Fig.7 Comparison of the γ_c from LVDT and IP considering the sections monitored

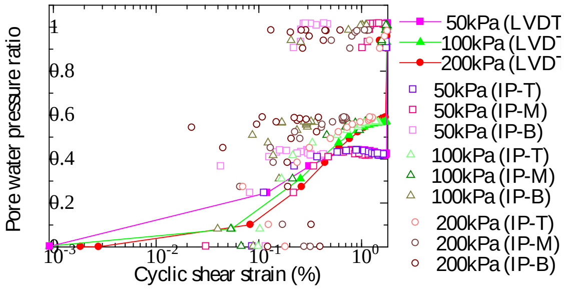

Fig.8 Pore water pressure and γ_c plot for 2.4 mm SA

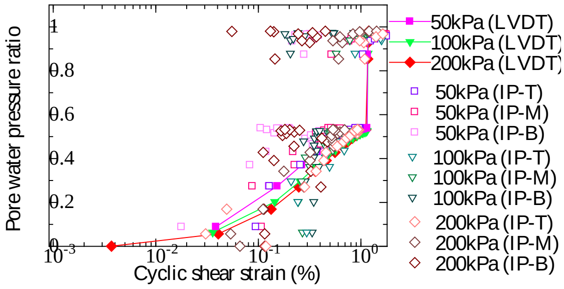

Fig.9 Pore water pressure and γ_c plot for 1.6 mm SA

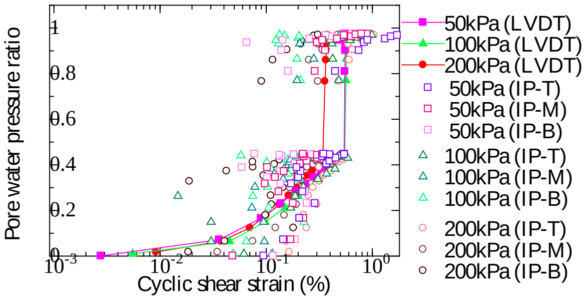

Fig.10 Pore water pressure and γ_c plot for 0.8 mm SA

For the results of the γ_{cl}, the estimated values from IP are tabulated in Table 2. Based on the results, a range of values was estimated from the location and sections monitored. At 2.4 mm SA, the values estimated at the top section were larger when compared to the other locations and conditions. For the 1.6 and 0.8 mm SA, a decrease in minimum values was observed. The changes in values can be attributed to the amount of cyclic deformation applied to the sample. Larger values were applied to 2.4 mm SA and this can result in more deformation with respect to the x and y-directions as the sample is being cyclically loaded. The effect of increasing the confining pressure was also investigated. Increasing the confining pressure caused a decrease in value at the top section for all locations monitored. For the middle and bottom section, a decrease in the maximum values was observed. The results from IP were compared to the computed shear strains from the LVDT. As seen in Table 2, the values at 2.4 mm SA had larger results. This trend was also observed for the results IP. Comparing the results, most of the computed values from the LVDT were within the range of the values from IP. As a whole, values estimated from IP are smaller for the minimum values while larger for maximum values.

Table 2 γ_{cl} for S1 (%) estimated from IP

SA	Loc	Cell Pressure (kPa)		
		50	100	200
2.4	T	1.356 - 2.383	1.545 - 2.281	0.955 - 1.509
	M	0.526 - 1.160	0.547 - 2.105	0.198 - 1.105
	B	0.031 - 0.431	0.037 - 4.387	0.153 -0.596
1.6	T	1.014 - 2.376	1.212 - 2.063	0.574 -1.621
	M	0.381 - 1.416	0.488 -1.299	0.218 -1.076
	B	0.014 - 0.534	0.186 - 0.596	0.009 - 3.546
0.8	T	0.756 - 1.414	0.248 - 0.948	0.103 - 0.519
	M	0.062 - 1.135	0.135 - 4.078	0.006 - 3.835
	B	0.020 - 1.643	0.046 - 0.463	0.066 - 0.260

The results were also compared to the typical values of γ_{cl}. Typical values ranges from 0.4-3% [8].The minimum values for all conditions are within the range but the maximum values are larger. Larger values are normally obtained at the middle section and the outer edge of the bottom section. For the behavior of the excess pore water pressure, its development was observed to be different for all the strain amplitudes tested. At higher SA, the excess pore water pressure rapidly developed and this was followed by the occurrence of liquefaction. When the confining pressure was increased, the void spaces within the sample decreased which resulted in a slow development of the excess pore water pressure**.**

Table 3 γ_{cl} for S1 (%) for S1 from LVDT

SA	Cell Pressure (kPa)		
	50	100	200
2.4	1.718	1.707	1.506
1.6	1.088	1.108	1.387
0.8	0.487	0.380	0.044

To further investigate on the difference between the results of the different locations and sections monitored, the shear strain field color map was extracted. Typical results are presented in Fig.11. The color maps presented are obtained from the first cycle and they show the development of the shear strain starting at the early stages of the compression phase towards the extension phase. The 80th and 185th seconds are the peak at compression and extension, respectively. It can be seen that there is a non-homogeneous distribution. This is the reason of having a range of estimated values for the γ_{cl}. The values at the top are larger compared to the bottom section. The middle section had a scatter of larger values. It is in this section where larger values were estimated when compared to the typical values. The results of the displacement fields in both x and y-directions were also plotted on a color map. The typical results for the displacement field in the y-direction (VDF) can be seen in Figs.12-13. In the color map, positive values indicate a downward movement while negative values indicate upward movements. The displacement fields presented in Fig.12 is at the first cycle and the 80th and 185th seconds are the peak at compression (CL) and extension (EL) loading, respectively. It can be observed that at the 45th seconds the critical area or the area where large displacement concentration occurred was initially seen at near the top cap. This critical area was also visible for both peak CL and EL. Liquefaction happened towards the end of the first cycle. When it happened, its influence on the sample's behavior can be seen in the succeeding cycle. At Fig.13, the critical area appeared to have more deformation at 45th seconds when compared to the previous cycle. At the 80th seconds or peak at CL, the deformation at the critical area similarly became larger. For the 185th seconds or peak at EL, a deformation at the critical area suddenly decreased. Furthermore, as the sample was being compressed it can be seen that the middle section had scattered large deformation as well. The bottom section consistently had small values. Deformation behavior changed once liquefaction had happened. A typical result is seen in Figs.14-15. These were taken at the peak state of the CL and EL, respectively. It can be seen that as liquefaction occurs the critical area propagated at a deeper depth. For the EL, the critical area became smaller and towards the end of the cyclic loading, it disappears. After liquefaction had triggered, the critical area appeared at different loading conditions. Initially, it occurs at the CL then it shifts to the EL.

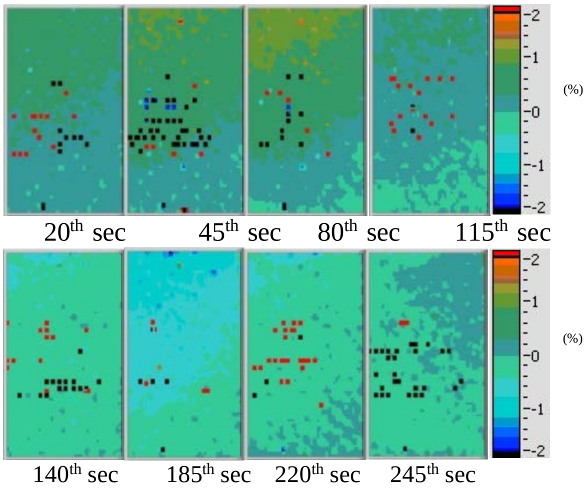

20th sec 45th sec 80th sec 115th sec

140th sec 185th sec 220th sec 245th sec

Fig.11 Shear strain map for S1

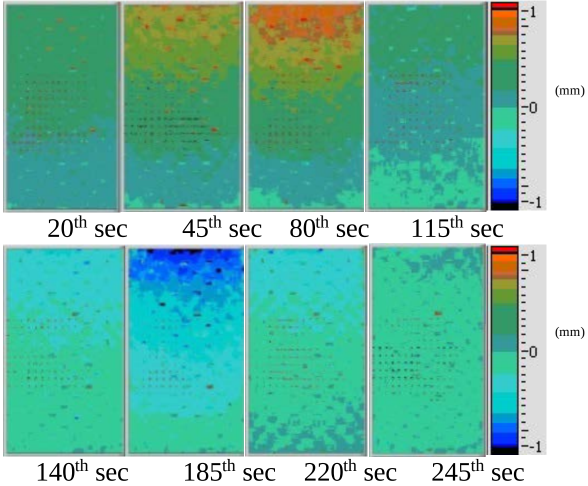

20th sec 45th sec 80th sec 115th sec

140th sec 185th sec 220th sec 245th sec

Fig.12 VDF of S1 at the first cycle for the y-direction

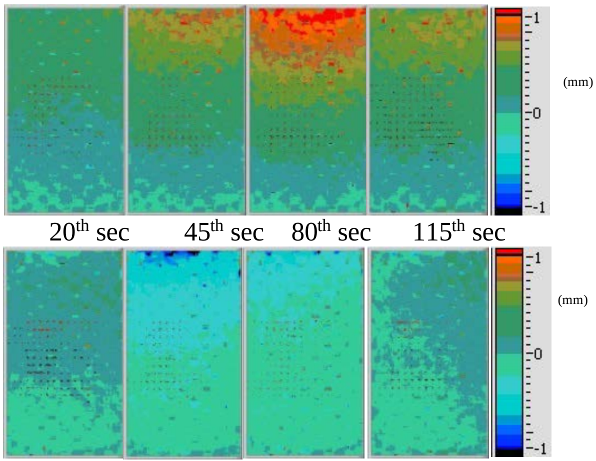

20th sec 45th sec 80th sec 115th sec

140th sec 185th sec 220th sec 245th sec

Fig.13 VDF of S1 at the second cycle for the y-direction

For the behavior of the soil with respect to the horizontal direction (HDF), the typical results are shown in Figs.16-17. Positive values indicate that the sample moved towards the right. Negative values indicate that the sample towards the left. The color maps were taken from the peak state of the CL and EL. For the peak at CL as seen in Fig.15, at the first cycle, the left side of the sample tends to move towards the left. The right side of the sample moved towards the right. This can be an indication that expansion happened during compression. Once liquefaction occurred, the behavior gradually changed to tilting towards the right side. For the peak at EL as seen in Fig.16, at the first cycle contraction was observed on the left side of the sample moved towards the right while the other side moved towards the left. Similarly, after liquefaction had occurred, the behavior changed to tilting towards the right side.

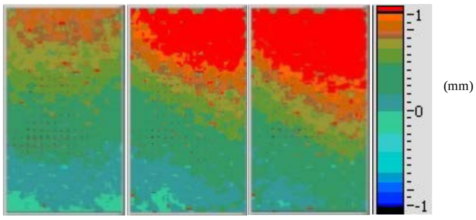

Cycle 1 Cycle5 Cycle 10

Fig.14 VDF of S1 at peak for the CL

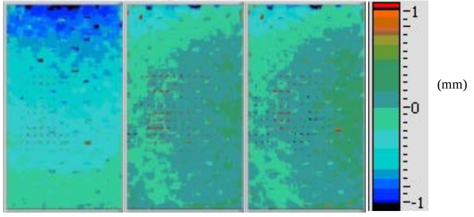

Cycle 1 Cycle5 Cycle 10

Fig.15 VDF of S1 at peak for the EL

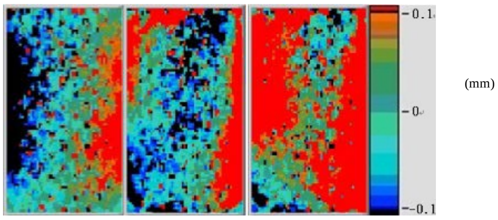

Cycle 1 Cycle5 Cycle 10

Fig.16 HD field of S1 at the peak for the CL

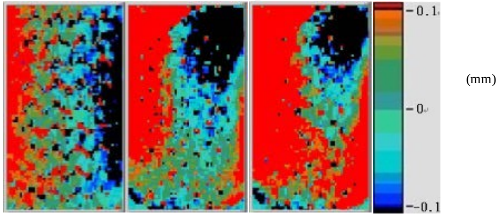

Cycle 1 Cycle5 Cycle 10

Fig.17 HD field of S1 at the peak for the EL

6. CONCLUSION

The cyclic shear strain that would trigger liquefaction was estimated using image processing. The computed cyclic shear strain from image processing was first compared with the results from the LVDT. There was a good agreement with the target chosen with values from the LVDT. For the internal measurement, the values were larger at the top compared to the middle and bottom sections. The cyclic shear strain that would trigger liquefaction computed from the LVDT was also compared with image processing. From the range of estimated values from image processing, the minimum values were found to be smaller while the maximum values were larger. When the values were compared to typical results, the minimum values are in agreement but the maximum values were larger. Based on the results of the estimation the parameter was observed to be affected by the strain amplitude and confining pressure. From the technique, it was determined that the values of the cyclic shear strain that would trigger liquefaction vary with the location it was obtained because of the existence of non-homogeneous movement in the soil. Image processing was also adopted to monitor the triggering of liquefaction. The monitoring was performed by extracting the displacement field with respect to the x and y-directions and the shear strain field. It was observed that deformation behavior was different before, during and after the occurrence of liquefaction. Before liquefaction, the critical area begins to appear for both compression and extension loading. During liquefaction, a similar behavior before liquefaction occurred was observed. It was after liquefaction had happened that its effect was noticed. A shift in the occurrence of the critical area was observed when liquefaction had occurred. This shift signifies that the behavior of the soil becomes weaker and more vulnerable as it is being liquefied. From the technique, the early detection of the critical zones was observed. The applied technique in monitoring the triggering of liquefaction has the potential to be implemented in other laboratory tests such as shaking table test. Furthermore, it can still be extended to three-dimensional monitoring. This can be useful in extracting the volume changes of a soil under loading.

7. ACKNOWLEDGMENTS

The researcher would like to express her deep gratitude towards the Engineering Research and Development for Technology (ERDT) scholarship for funding the research. The researcher would also like to thank the Civil Engineering Department of De La Salle University and the Graduate School of Civil and Environmental Engineering of Nagoya University Geotechnical Engineering Division for their support in the research.

8. REFERENCES

[1] Marto A., Tan, C.S., Makhtar, A.M., and Jusoh, S.N., Cyclic Behaviour of Johor Sand. International Journal of GEOMATE, Vol. 10, Issue 21, 2016, pp. 1891-1898.

[2] Wu J., Kammerer A.M., Riemer M.F., Seed R.B. and Pestana J.M., Laboratory Study of Liquefaction Triggering Criteria. Thirteenth World Conferences on Earthquake Engineering (WCEE), 2004.

[3] Kusumawardani R., Suryolelono K.B., Suhendro B. and Rifa'i A. Dynamic Behaviour of Yogyakarta’s Sand under Cyclic Triaxial Testing. International Journal of Civil & Environmental Engineering, Vol. 13, Issue 2, 2013, pp. 23-28.

[4] Dobry R. and Abdoun, T., Recent Findings on Liquefaction Triggering in Clean and Silty Sands during Earthquakes. Journal of Geotechnical and Geoenvironmental Engineering, Vol. 143, Issue 10, 2017, pp. 04017077-1-19.

[5] Cetin K.O., Seed R.B., Kiureghian, A.D., Tokimatsu K., Harder Jr. L.F., Kayen R.E. and Moss R.E., Standard Penetration Test-Based Probabilistic and Deterministic Assessment of Seismic Soil Liquefaction Potential. Journal of Geotechnical and Geoenvironmental Engineering, Vol. 130, Issue 12, 2004, pp.1314-1340.

[6] Seed H.B., Idriss I.M. and Arango I., Evaluation of Liquefaction Potential Using Field Performance Data. Journal of Geotechnical Engineering, Vol. 109, Issue 3, 1983, pp. 458-482.

[7] Dobry R. and Abdoun T., An Investigation into Why Liquefaction Charts Work: A Necessary Step Toward Integrating the States of Art and Practice. Proceedings of the Fifth International Conference on Earthquake Geotechnical Engineering, 2011, pp. 13-45.

[8] Dobry R. and Abdoun T., Cyclic Shear Strain Needed for Liquefaction Triggering and Assessment of Overburden Pressure Factor Kσ. ASCE Journal of Geotechnical and Geoenvironmental Engineering, 2015, pp. 1-18.

[9] Uy E.E.S. and Boonyatee T., Image Processing for Geotechnical Laboratory Measurements. International Journal of GEOMATE, Vol. 10, Issue 22, 2016, pp. 1964-1970.

[10] Viggiani G. and Hall S.A., Full-Field Measurements, A New Tool For Laboratory Experimental Geomechanics. Proceedings of the 4th International Symposium on Deformation Characteristics of Geomaterials (Burns SE, Mayne PW and Santamarina JC (Eds.)), 2008.

[11] Xing Z.X., Wells L.G., Yaping J. and Shearer S.A., Using Image Analysis to Measure Two-Dimensional Soil Deformation. Journal of Terramechanics. Vol. 34, Issue 2, 1997, pp. 73-82.

[12] Longtan S., Song Y., Yong S., Chuan, H. and Xiaoxia, G., Application of Digital Image Processing Technology in Dynamic Triaxial Test of Soil Mechanics. Journal of Theoretical and Applied Information Technology, Vol. 48, Issue 3, 2013, pp.1358-1365.

[13] Koseki J., Hoshino R., Miyashita Y. and Sato T., Direct and Indirect Observations of Local Properties of Saturated Sand Specimens in Undrained Cyclic Triaxial Tests. The 6th Japan-Korea Geotechnical Workshop, Vol. 4, Issue 1, 2016.

[14] Kaler P. Study of Grayscale Image in Image Processing. International Journal on Recent and Innovation Trends in Computing and Communication. Vol. 4, Issue 11, 2016, pp. 309-311.

[15] Wedel A. and Cremers D., Stereo Scene Flow for 3d Motion Analysis. Vol. 9, 2011.

[16] Thota S.D., Vemulapalli K.S., Chintalapati K. and Srinivas, P.S., Comparison Between the Optical Flow Computational Techniques. International Journal of Engineering Trends and Technology, Vol. 4, Issue 10, 2013.

[17] Fernando W.S.P., Udawatta L. and Pathirana P., Identification of Moving Obstacles with Pyramidal Lucas and Kanade Optical Flow and K Means Clustering. Proceedings of the 2007 Third International Conference on Information and Automation for Sustainability, 2007.

[18] Bradski G. and Kaehler A., Learning Opencv Computer Vision with The Opencv Library. O’Reilly, 2008.

[19] The Japanese Geotechnical Society, Japanese Geotechnical Society Standards: Laboratory Testing Standards of Geomaterial. Issue 1, 2008.

[20] Sutton M.A., Orteu J.J. and Schreier H.W., Image Correlation for Shape, Motion and Deformation Measurements: Basic Concepts, Theory and Applications: Springer, 2009. Vol.25, No.3, 2011, pp.1460-1465.